NAWCWPNS TP 8318

# A Real-Space, Modal-Expansion Method With the R-Matrix Propagator To Calculate Grating Diffraction

by
J. Merle Elson
and
P. Tran
*Research and Technology Division*

**SEPTEMBER 1996**

**NAVAL AIR WARFARE CENTER WEAPONS DIVISION**
**CHINA LAKE, CA 93555-6100**



Approved for public release; distribution is unlimited.

# Naval Air Warfare Center Weapons Division

## FOREWORD

This work was supported in part by a grant of High Performance Computing Center, time from the DOD U.S. Army Corps of Engineers Waterways Experiment Station (Cray Research C-916 and Y-MP). The authors were supported by Navy In-House Laboratory Independent Research funds.

This report is a working document subject to change and was reviewed for technical accuracy by Brett Borden.

Approved by
R. L. Derr, *Head*
*Research and Technology Division*
5 September 1996

Under authority of
J. V. Chenevey
Capt., U.S. Navy
*Commander*

Released for publication by
S. HAALAND
*Director for Research and Engineering*

NAWCWPNS Technical Publication 8318

Published by . . . . . Technical Information Division
Collation . . . . . Cover, 9 leaves
First printing . . . . . 45 copies

# REPORT DOCUMENTATION PAGE

*Form Approved*
*OMB No. 0704-0188*



| 1. AGENCY USE ONLY *(Leave blank)* | 2. REPORT DATE | 3. REPORT TYPE AND DATES COVERED |
|---|---|---|
| | September 1996 | Interim report - October 1995-September 1996 |

**4. TITLE AND SUBTITLE**
A Real-Space, Modal-Expansion Method With The R-Matrix Propagator To Calculate Grating Diffraction

**5. FUNDING NUMBERS**
N0001496WX20167

**6. AUTHOR(S)**
J. Merle Elson and P. Tran

**7. PERFORMING ORGANIZATION NAME(S) AND ADDRESS(ES)**
Naval Air Warfare Center Weapons Division
China Lake, CA 93555-6100

**8. PERFORMING ORGANIZATION REPORT NUMBER**
NAWCWPNS TP 8318

**9. SPONSORING/MONITORING AGENCY NAME(S) AND ADDRESS(ES)**
Office of Naval Research
ONR 354-Dr. Ronald Kostoff
Ballston Tower One
800 N. Quincy St.
Arlington, VA 22217-5660

**10. SPONSORING/MONITORING AGENCY REPORT NUMBER**

**11. SUPPLEMENTARY NOTES**

**12A. DISTRIBUTION/AVAILABILITY STATEMENT**
A Statement; Distribution Unlimited

**12B. DISTRIBUTION CODE**

**13. ABSTRACT** *(Maximum 200 words)*

(U) Recently the **R**-matrix propagation algorithm has been used in conjunction with a *k*-space modal-expansion to calculate diffraction from gratings [J. M. Elson and P. Tran, *J. Opt. Soc. Am. A,* Vol. 12]. The **R**-matrix eliminates numerical instability associated with deep gratings. We introduce here a real-space version of the modal-expansion method. A detailed numerical study of the convergence versus number of diffracted orders is given. For wavelength $\lambda$, we consider sinusoidal gratings having height $h = 1.7\lambda$ and $17\lambda$ where both have period $d = 1.7\lambda$. We consider absorbing metallic and nonabsorbing dielectric gratings. Results are compared with those of other authors and with our previous results.

**14. SUBJECT TERMS**
Electromagnetic theory
Grafting diffraction
R-Matrix

**15. NUMBER OF PAGES**
16

**16. PRICE CODE**

| 17. SECURITY CLASSIFICATION OF REPORT | 18. SECURITY CLASSIFICATION OF THIS PAGE | 19. SECURITY CLASSIFICATION OF ABSTRACT | 20. LIMITATION OF ABSTRACT |
|---|---|---|---|
| UNCLASSIFIED | UNCLASSIFIED | UNCLASSIFIED | UL |

# INTRODUCTION

The **R**-matrix propagation technique has recently been introduced by several authors (References 1 through 6) as a means of removing the numerical instability encountered in calculating diffraction from deep gratings (depth $h >$ wavelength $\lambda$). The method was first described in the field of chemical physics (Reference 7). The idea is to find a quantity called **R** that describes the relationship between some field quantity and its derivative. When the field has exponential behavior, $\exp(\alpha z)$, the quantity **R** will be proportional to $\alpha z$ and will not suffer from exponential instability. Applying this idea to such a relationship in the theory of grating diffraction, the method seeks a matrix that relates the electric field on both sides of a layer to the magnetic field on both sides. This method on the **R**-matrix method is unlike the **T**-matrix propagation method that seeks a matrix relating the electric and magnetic field on one side of a layer to the electric and magnetic field on the other side of a layer.

In References 1 and 2, diffraction calculations were performed for nonabsorbing dielectric and absorbing metallic sinusoidal gratings with period $d = 1.7\lambda$ and heights $h = 0.17,\ 1.7,\ 17,$ and $170\lambda$ for both transverse-electric (TE) and transverse-magnetic (TM) polarization. The results were compared with other methods where applicable. The performance of the **R**-matrix method was good in all cases except for TM polarization and metallic gratings with $h \geq 17\lambda$. These cases suffered from poor convergence where the diffraction efficiency fluctuated with the number of orders kept in the expansion.

In Reference 1, the **R**-matrix method was used in conjunction with a multilayer-modal expansion to calculate the diffraction efficiency. The grating is subdivided into many sublayers such that within each sublayer, the permittivity can be approximated as constant across the sublayer. In the dimensions parallel to the boundaries of a sublayer, the permittivity and the fields are expanded in a Fourier series. Within each sublayer, the Fourier components of the permittivity are known, and the Fourier components of the field are determined from a set of linear equations.

In this work, we do not expand the permittivity and fields in each sublayer into Fourier components. Instead, we will solve for the fields in real space. The motivation for this approach is to try to circumvent the slow convergence of a Fourier expansion when there are one or more sharp discontinuities in the quantity being expanded. These discontinuities include the field across a boundary or the sharp jump in the dielectric permittivity. It is not clear to the authors why metallic permittivities and TM polarization appear to present the greatest problem in this regard. Nevertheless, this problem has motivated taking the present real space approach where series representation of discontinuities in permittivity is not an issue.

The method described here is similar to that described in References 3 and 4 where the authors mainly looked at transmission and band structure of a bulk photonic crystal and dispersion of surface modes propagating along the surface of a truncated photonic crystal. These calculations were for nonabsorbing dielectric materials. In this paper, we will focus on the gratings considered in References 1 and 2. The next section briefly describes the method used in this work. Additional details can be found in References 1, 3, and 4. Numerical results along with convergence data are presented.

## METHOD OF CALCULATION

In Figure 1, a sinusoidal profile with nomenclature is shown. We assume the grating profile is infinitely periodic in the $\hat{\mathbf{x}}$ direction, uniform in the $\hat{\mathbf{y}}$ direction, and with peak-to-valley height $h = z_2 - z_1$ in the $\hat{\mathbf{z}}$ direction. The grating is illuminated by a plane wave of wavelength $\lambda$ with wave vector in the $(\hat{\mathbf{x}},\hat{\mathbf{z}})$ plane. There are three general regions of interest: the homogeneous superstrate, the homogeneous substrate, and the finite thickness region in between containing the grating profile. The superstrate has permittivity $\varepsilon_{inc}$ and contains the incident and reflected fields. The substrate has permittivity $\varepsilon_{sub}$ and contains the transmitted field. The profile region in between is described by a spatially variable permittivity $\varepsilon(\mathbf{r})$ where $\mathbf{r} = (x, z)$ and $z_1 \le z \le z_2$.

In Figure 1, a sinusoidal profile is subdivided into $n_z$ layers each having uniform thickness $\Delta z = h / n_z$. Even though the grating profile region is generally divided into sublayers, the number $n_z$ of sublayers can range from 1 to much greater than 1. For a given height $h$, the number $n_z$ obviously relates to thickness $\Delta z$, and the main criterion for $\Delta z$ is the requirement that the permittivity within each sublayer can be treated as independent of $z$. For example, a rectangular profile need not be subdivided ($n_z$=1) regardless of height $h$. However, for a sinusoidal profile, it is normally necessary to subdivide into $n_z >> 1$ layers to achieve a reasonably accurate profile shape and sublayers which are approximately independent of $z$. Even though we assume each sublayer has constant thickness $\Delta z$, this assumption is not necessary.

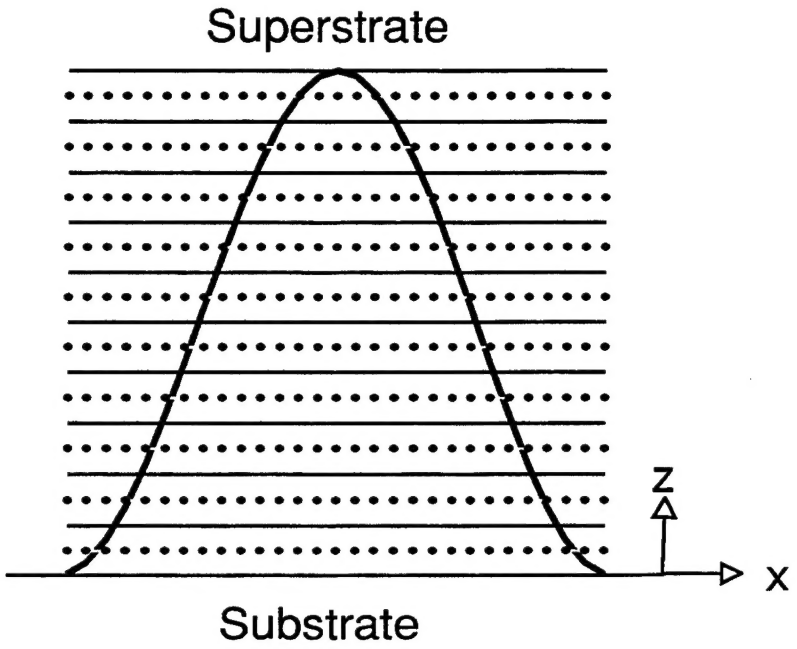


FIGURE 1. Schematic of Sinusoidal Profile Versus One Period Showing $x$-Coordinate Discretization and Sublayer Divisions. In this example, the dots indicate discretization of the $x$-dimension over one period $d$ into $n_x = 29$ points. The number of divisions of grating height $h$ is $n_z = 10$, as shown by the horizontal solid lines. The area under the sine curve contains substrate material. Each dot lying under the sine curve represents an $x$-point where the permittivity is that of the substrate. Likewise, each dot above the sine curve is an $x$-point with superstrate permittivity. Each adjacent pair of horizontal solid lines represents a sublayer, and the dotted line in between also denotes the center-$z$ coordinate $z_c$ for that sublayer.

We wish to solve the two Maxwell's equations $\nabla \times \mathbf{E}(\mathbf{r}) = i(\omega/c)\mathbf{H}(\mathbf{r})$ and $\nabla \times \mathbf{H}(\mathbf{r}) = -i(\omega/c)\varepsilon(\mathbf{r})\mathbf{E}(\mathbf{r})$ within a given sublayer. To do this, we write the $x$-dependence of these two equations as a centered finite-difference approximation. The $x$-coordinate is discretized over period $d$ into $n_x$ points each uniformly separated by $\Delta x = d/n_z$. For a layer bounded from $z \rightarrow z + \Delta z$, we eliminate the $z$-component of the electric and magnetic fields and obtain four equations relating the $\hat{\mathbf{x}}$ and $\hat{\mathbf{y}}$ field components:

$$\frac{\partial E_x(x,z)}{\partial z} = \frac{i\omega}{c} H_y(x,z)$$

$$+ \frac{ic}{\omega(\Delta x)^2} \left\{ \frac{H_y(x+\Delta x,z) - H_y(x,z)}{\varepsilon(x+\Delta x/2, z_c)} + \frac{H_y(x-\Delta x,z) - H_y(x,z)}{\varepsilon(x-\Delta x/2, z_c)} \right\} \quad \text{(1a)}$$

$$\frac{\partial E_y(x,z)}{\partial z} = -\frac{i\omega}{c} H_x(x,z) \tag{1b}$$

$$\frac{\partial H_x(x,z)}{\partial z} = -\frac{i\omega}{c}\varepsilon(x,z_c)E_y(x,z) + \frac{ic}{\omega(\Delta x)^2}\left\{2E_y(x,z) - E_y(x+\Delta x,z) - E_y(x-\Delta x,z)\right\} \tag{1c}$$

$$\frac{\partial H_y(x,z)}{\partial z} = \frac{i\omega}{c}\varepsilon(x,z_c)E_x(x,z) \tag{1d}$$

In Equations 1a and 1c, the finite-difference centered derivative approximations on the right-hand sides are accurate to $O(\Delta x^2)$. As shown in the Appendix, we have also considered approximations, which are accurate to $O(\Delta x^4)$ (shown in the Appendix). We have evaluated the permittivity $\varepsilon$ at $z = z_c$, which represents the center $z$-coordinate of the sublayer. Since the sublayer is bounded from $z$ to $z+\Delta z$, it follows that $z_c = z + \Delta z/2$. Because of this, these coupled differential equations have coefficients which are independent of $z$ for a given sublayer. When all $n_x$ discrete $x$-coordinates (denoted by $\mathbf{X}$) are included, the coupled set of differential equations in Equation 1 may be written in matrix form as

$$\frac{\partial}{\partial z}\begin{pmatrix} E_x(\mathbf{X},z) \\ E_y(\mathbf{X},z) \\ H_x(\mathbf{X},z) \\ H_y(\mathbf{X},z) \end{pmatrix} = \mathbf{M}(\mathbf{X},z_c)\begin{pmatrix} E_x(\mathbf{X},z) \\ E_y(\mathbf{X},z) \\ H_x(\mathbf{X},z) \\ H_y(\mathbf{X},z) \end{pmatrix} \tag{2}$$

Since $\mathbf{M}$ is independent of $z$ within the sublayer, the modal solution is straightforward by diagonalization of $\mathbf{M}$ and, in the original basis set, this solution has the form

$$\begin{pmatrix} E_x(\mathbf{X},z) \\ E_y(\mathbf{X},z) \\ H_x(\mathbf{X},z) \\ H_y(\mathbf{X},z) \end{pmatrix} = \begin{pmatrix} S_{11} \\ S_{21} \\ \vdots \\ S_{N1} \end{pmatrix}\exp(\lambda_1 z)C_1 + \begin{pmatrix} S_{12} \\ S_{22} \\ \vdots \\ S_{N2} \end{pmatrix}\exp(\lambda_2 z)C_2 + \cdots + \begin{pmatrix} S_{1N} \\ S_{2N} \\ \vdots \\ S_{NN} \end{pmatrix}\exp(\lambda_N z)C_N \tag{3a}$$

where $N = 4n_x$. The column vectors on the right-hand side are eigenvectors of the matrix $\mathbf{M}(\mathbf{X}, z_c)$, and the $\lambda_j$, $j = 1, 2, \cdots, N$ are the associated eigenvalues. The $C_j$ are constants. Equation 3a may be compactly written in matrix form as

$$\begin{pmatrix} E_x(\mathbf{X},z) \\ E_y(\mathbf{X},z) \\ H_x(\mathbf{X},z) \\ H_y(\mathbf{X},z) \end{pmatrix} = \mathbf{S}(\mathbf{X},z_c)\mathbf{exp}(\Lambda z)\mathbf{C} \quad . \tag{3b}$$

The $\mathbf{S}(\mathbf{X},z_c)$ is a square matrix having columns which are the eigenvectors of $\mathbf{M}(\mathbf{X},z_c)$. The $\mathbf{exp}(\Lambda z)$ is a diagonal matrix of exponential terms with $\Lambda$ representing the set of eigenvalues associated with $\mathbf{M}(\mathbf{X},z_c)$, and $\mathbf{C}$ is a column vector of constants $C_j$.

In constructing the matrix $\mathbf{M}$, field terms in Equations 1a and 1c with extreme $x$-values $(x \pm \Delta x)$, which fall outside the dimension of one period are "wrapped around" by using the Floquet relationship. Because the only part of Equation 1 that depends on the grating profile is the permittivity $\varepsilon(\mathbf{r})$, the task of describing various profile shapes is straightforward, and typically only minor changes to computer algorithms are required.

From Equation 3b, we may form a relationship which is the essence of the **R**-matrix algorithm

$$\begin{pmatrix} E_x(\mathbf{X},z) \\ E_y(\mathbf{X},z) \\ E_x(\mathbf{X},z+\Delta z) \\ E_y(\mathbf{X},z+\Delta z) \end{pmatrix} = \mathbf{r}(\Delta z) \begin{pmatrix} H_x(\mathbf{X},z) \\ H_y(\mathbf{X},z) \\ H_x(\mathbf{X},z+\Delta z) \\ H_y(\mathbf{X},z+\Delta z) \end{pmatrix} \tag{4}$$

This is accomplished by combining Equation 3b evaluated at $z$-values of $z$ (as shown) and $z + \Delta z$ to eliminate $\mathbf{C}$ and rearranging the result to have the form given in Equation 4. This matrix equation defines the sublayer **r**-matrix and is basic to the **R**-matrix algorithm. The **r**-matrix must be calculated for each sublayer. We compare the **r**-matrix definition to the corresponding definition for a sublayer **t**-matrix which we write as

$$\begin{pmatrix} E_x(\mathbf{X},z) \\ E_y(\mathbf{X},z) \\ H_x(\mathbf{X},z) \\ H_y(\mathbf{X},z) \end{pmatrix} = \mathbf{t}(\Delta z) \begin{pmatrix} E_x(\mathbf{X},z+\Delta z) \\ E_y(\mathbf{X},z+\Delta z) \\ H_x(\mathbf{X},z+\Delta z) \\ H_y(\mathbf{X},z+\Delta z) \end{pmatrix} \tag{5}$$

The elements of the **t**-matrix contain terms which behave exponentially as $\exp(\pm\alpha\Delta z)$ where $\alpha$ is complex, and $\Delta z$ is the thickness of the sublayer. When the real part of the product $\alpha\Delta z$ is large, numerical problems with exponential overflow and underflow will likely occur. Even if the real part of $\alpha\Delta z$ is small for any sublayer, propagation through many sublayers by means of products of **t**-matrices will cause the exponential behavior to accumulate with the number of sublayers, which will eventually lead to numerical instability. On the other hand, the elements of the **r**-matrix have a linear dependence on $\pm\alpha\Delta z$, and this behavior, which is a vast improvement over exponential, will be much more numerically tractable for propagation through many sublayers.

Returning to Equation 4, note that if $\Delta z$ is the full thickness $h$ of the profile region (for example, a rectangular profile), then no further propagation through the profile region is necessary because the fields have been related by $\mathbf{r}(\Delta z)$ across $h = z_2 - z_1$. For more general profile shapes, more sublayers are needed. Then it is necessary to relate the field solutions obtained in each sublayer of thickness $\Delta z$ that subdivides $h = z_2 - z_1$. To this end, we also assume that a relation analogous to Equation 4 exists that covers the entire grating height $h = z_1 - z_2$. We express this relationship as

$$\begin{pmatrix} E_x(\mathbf{X},z_1) \\ E_y(\mathbf{X},z_1) \\ E_x(\mathbf{X},z_2) \\ E_y(\mathbf{X},z_2) \end{pmatrix} = \begin{pmatrix} \mathbf{R}_{11}(z_2-z_1) & \mathbf{R}_{12}(z_2-z_1) \\ \mathbf{R}_{21}(z_2-z_1) & \mathbf{R}_{22}(z_2-z_1) \end{pmatrix} \begin{pmatrix} H_x(\mathbf{X},z_1) \\ H_y(\mathbf{X},z_1) \\ H_x(\mathbf{X},z_2) \\ H_y(\mathbf{X},z_2) \end{pmatrix} \tag{6}$$

where the global **R**-matrix, $\mathbf{R}(z_2 - z_1)$, is written in a sectored form. The matrices $\mathbf{R}_{11}$, $\mathbf{R}_{12}$, $\mathbf{R}_{21}$, and $\mathbf{R}_{22}$ are computed by means of a recursive algorithm, and further details are given in References 1 through 3. To initialize the recursion relations, we see from Equations 4 and 6 that we may set $z_2 = z_1 + \Delta z_1$, and therefore $\mathbf{R}(\Delta z_1) = \mathbf{r}(\Delta z_1)$. With this initialization, successive applications of the recursive algorithm yields $\mathbf{R}(\Delta z_1 + \Delta z_2)$, $\mathbf{R}(\Delta z_1 + \Delta z_2 + \Delta z_3)$, ''', $\mathbf{R}(\Delta z_1 + \Delta z_2 + \Delta z_3 + \cdots + \Delta z_{n_z})$ where $\Delta z_1 + \Delta z_2 + \Delta z_3 + \cdots + \Delta z_{n_z} = z_2 - z_1$ and the $\Delta z_j$ can be different.

Given the **R**-matrix and a few more intermediate steps, we can arrive at the final relationship from this calculation the relative amount of energy diffracted into the substrate and superstrate. To do this, we convert the fields to $k$-space by applying a Fourier transform matrix to Equation 6. This step is advantageous because in $k$-space we can relate the electric and magnetic fields in the homogeneous substrate and superstrate (which will be important later in Equation 9). Another advantage is that grating diffraction is conveniently expressed in $k$-space. The Fourier transform matrix $\mathbf{F}(\mathbf{K},\mathbf{X})$ is discretized consistent with the $r$-space digitization earlier and for electric fields we have

$$\mathbf{F}(\mathbf{K},\mathbf{X})\begin{pmatrix} E_x(\mathbf{X},z_1) \\ E_y(\mathbf{X},z_1) \\ E_x(\mathbf{X},z_2) \\ E_y(\mathbf{X},z_2) \end{pmatrix} = \begin{pmatrix} E_x(\mathbf{K},z_1) \\ E_y(\mathbf{K},z_1) \\ E_x(\mathbf{K},z_2) \\ E_y(\mathbf{K},z_2) \end{pmatrix} \tag{7}$$

and similarly for the magnetic field. The vector **K** denotes the set of wave vectors in $k$-space, and the number of $x$-points $n_x$ is identical to the number of diffracted orders in the set **K**. We apply this **F** matrix to Equation 6, which yields

$$\begin{pmatrix} E_x(\mathbf{K},z_1) \\ E_y(\mathbf{K},z_1) \\ E_x(\mathbf{K},z_2) \\ E_y(\mathbf{K},z_2) \end{pmatrix} = \overline{\mathbf{R}}(z_2 - z_1)\begin{pmatrix} H_x(\mathbf{K},z_1) \\ H_y(\mathbf{K},z_1) \\ H_x(\mathbf{K},z_2) \\ H_y(\mathbf{K},z_2) \end{pmatrix} \tag{8}$$

where $\overline{\mathbf{R}} = \mathbf{FRF}^{-1}$. Since the $z_1$ and $z_2$ are the substrate and superstrate boundaries, respectively, we can use the boundary conditions to relate the substrate and superstrate fields. From Equation 8, we find

$$\begin{pmatrix} E_x{}^t(\mathbf{K},z_1) \\ E_y{}^t(\mathbf{K},z_1) \\ E_x{}^r(\mathbf{K},z_2) + E_x{}^{inc}(\mathbf{K}^{inc},z_2) \\ E_y{}^r(\mathbf{K},z_2) + E_y{}^{inc}(\mathbf{K}^{inc},z_2) \end{pmatrix} = \overline{\mathbf{R}}(z_2 - z_1)\begin{pmatrix} H_x{}^t(\mathbf{K},z_1) \\ H_y{}^t(\mathbf{K},z_1) \\ H_x{}^r(\mathbf{K},z_2) + H_x{}^{inc}(\mathbf{K}^{inc},z_2) \\ H_y{}^r(\mathbf{K},z_2) + H_y{}^{inc}(\mathbf{K}^{inc},z_2) \end{pmatrix} \tag{9}$$

where $\mathbf{K}^{inc}$ is the in-surface incident beam wave vector. The incident beam electric and magnetic fields are described by $\mathbf{E}^{inc} = (E_x{}^{inc}, E_y{}^{inc})$ and $\mathbf{H}^{inc} = (H_x{}^{inc}, H_y{}^{inc})$. The superstrate and substrate media contain the reflected and transmitted fields, denoted by $r$ and $t$, respectively. At this point, a relation between the electric and magnetic fields can be easily obtained, and the calculation proceeds exactly as described previously (Reference 1, Equations 12 through 16).

## NUMERICAL RESULTS

The numercial results of this paper are an extension of Reference 1. This is because the numerical results of this work are also based on the same grating design parameters considered in References 1 and 2 but using a real-space modal expansion method. We will

compare some results of the present work with previous results by Li[2] and the authors' *k*-space approach. Figures 2 through 7 show our *r*-space convergence data for TM and TE polarization (electric field parallel and perpendicular to the plane of incidence) for three different gratings. The figures show relative intensity versus number of diffracted orders. The number of orders is equivalent to the number of discretized *x*-points $n_x$, which we choose to be an odd number, and the relative intensity refers to the ratio of diffracted power to incident power. For all the cases considered, the number of sublayers $n_z$ is 50, and the incident angle is 30 degrees.

In Figures 2 and 3, convergence data is shown for three reflected orders of an absorbing metallic grating $\varepsilon_{sub}$ = (−48.91, 4.2) with height $h = 1.7\lambda$ and period $d = 1.7\lambda$ ($h/d$=1). The data in Figures 2 (TM polarization) and 3 (TE polarization) indicate excellent convergence versus number of orders for this grating. For the same grating and TM polarization, Li[2] (Reference 2) reported that his method has poor convergence, because the results keep fluctuating with the number of orders. In Table 1, we compare the average value of the last five *r*-space data points shown in Figures 2 and 3 with previous results given in References 1 and 2. The agreement for TE polarization is very good. The agreement for TM polarization is poor, but that is to be expected, because the previous results have difficulty with convergence. For $h/d$ = 1, the present results compare well with the integral method and the method of fictitious sources (Reference 8), which gives TM-polarized reflection diffraction eeficiencies for the -2, -1, and 0 order as 0.197, 0.086, and 0595, respectively.

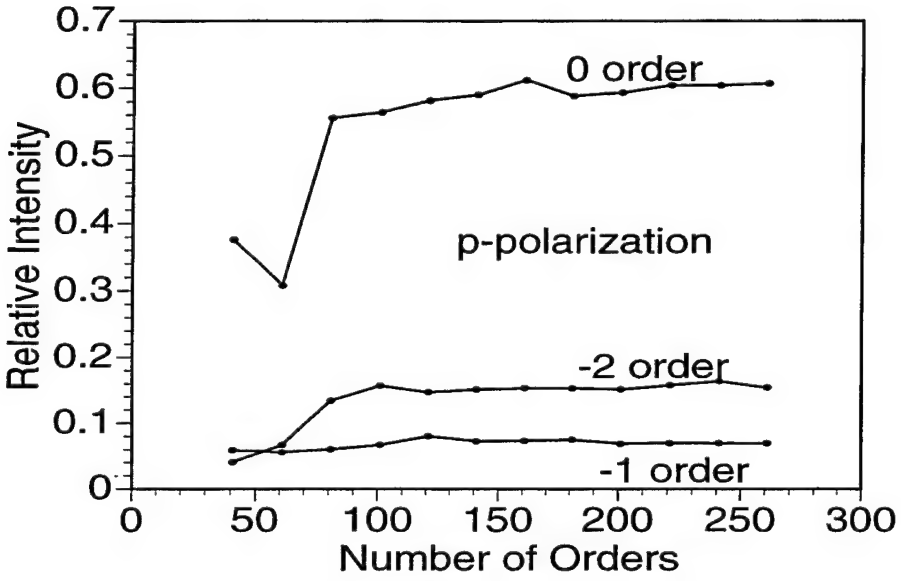


FIGURE 2. Relative TM-Polarized Diffraction Intensity of the Reflecting 0, −1, and −2 Orders Versus Number of Orders. The grating profile is sinusoidal, and the grating material is an absorbing metal with permittivity (−48.91, 4.2). The grating height is $h = 1.7\lambda$, period $d = 1.7\lambda$, angle of incidence 30 degrees, and the number of profile sublayers $n_z = 50$.

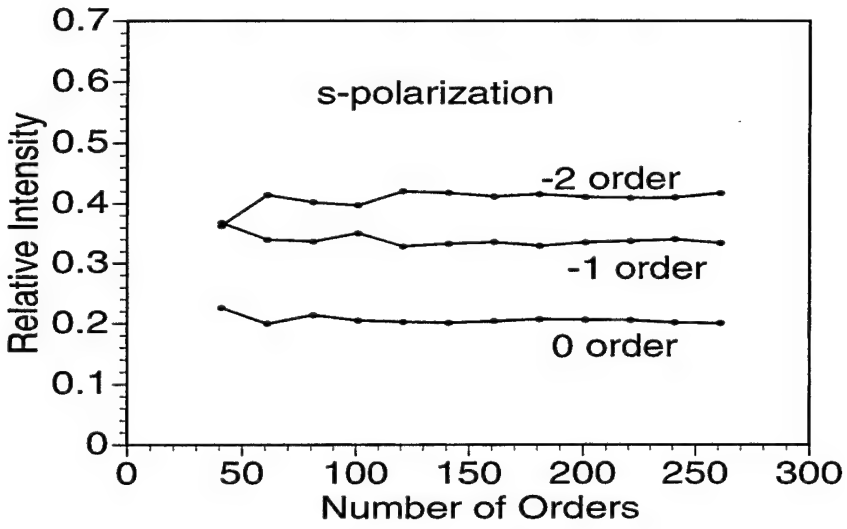


FIGURE 3. Relative TE-Polarized Diffraction Intensity of the Reflecting 0, -1, and -2 Orders Versus Number of Orders. This case is identical to Figure 2 except the incident beam is TE polarized.

TABLE 1. Reflection Diffraction Efficiencies Absorbing Metallic Sinusoidal Grating.

| | $h/d = 1$ | | | $h/d = 10$ | | |
|---|---|---|---|---|---|---|
| Order | 5-point *r*-space average | Our previous *k*-space | Li's | 5-point *r*-space average | Our previous *k*-space | Li's |
| TE polarization | | | | | | |
| -2 | 0.4122 | 0.4152 | 0.4135 | 0.1914 | 0.1885 | 0.1993 |
| -1 | 0.3348 | 0.3338 | 0.3353 | 0.1365 | 0.1353 | 0.1372 |
| 0 | 0.2039 | 0.2010 | 0.2018 | 0.3093 | 0.3086 | 0.3010 |
| TM polarization | | | | | | |
| -2 | 0.1560 | 0.0274 | 0.1264 | 0.2834 | 0.0160 | 0.0494 |
| -1 | 0.0705 | 0.0664 | 0.0603 | 0.0462 | 0.0078 | 0.3307 |
| 0 | 0.5993 | 0.2146 | 0.6609 | 0.1451 | 0.0315 | 0.1618 |

In Figures 4 and 5, we consider the same absorbing metallic grating except that the height is 10 times greater. The grating height $h$ is now $17\lambda$ ($h/d$ = 10) while the permittivity $\varepsilon_{sub}$ and period $d$ remain unchanged. Convergence data for the three reflected orders are shown in Figures 4 (TM polarization) and 5 (TE polarization). Both cases exhibit a "slow" damped oscillatory convergence. Note that solid and dotted curves are shown for each order. The solid curves are obtained from Equation 1, as shown, with the finite-difference approximation accurate to $O(\Delta x^2)$. The dotted curves are obtained from Equation 1 with a finite-difference approximation accurate to $O(\Delta x^4)$, as shown in the Appendix. The two methods show nearly identical results at larger order. This eliminates

the possibility of the finite-difference approximation being the cause of the slow convergence. At this point, we do not know the cause of the slow convergence. In the $h/d = 10$ column, Table 1 again compares the result with previous results from References 1 and 2. The agreement is excellent for TE polarization. For TM polarization, the previous results are not reliable as discussed in the last paragraph. There is no other exact result that can be used to check for this deep a grating.

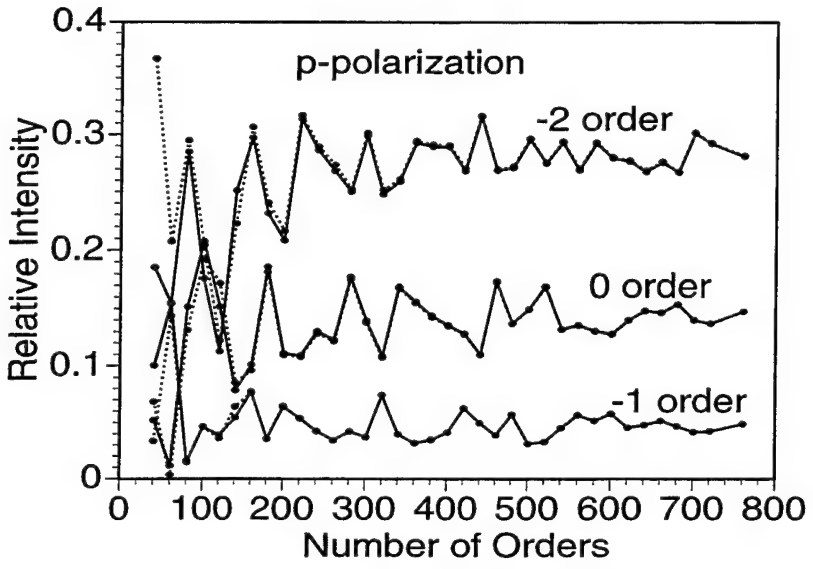


FIGURE 4. Relative TM-Polarized Diffraction Intensity of the Reflecting 0, −1, and −2 Orders Versus Number of Orders. The grating profile is sinusoidal, and the grating material is an absorbing metal with permittivity (−48.91, 4.2). The grating height is $h = 17\lambda$, period $d = 1.7\lambda$, angle of incidence 30 degrees, and the number of profile sublayers $n_z = 50$. This case is identical to Figure 2 except the grating height is 10 times larger. The solid and dotted lines, which are superimposed for the larger number of orders, are for finite-difference approximations accurate to $O(\Delta x^2)$ and $O(\Delta x^4)$, respectively.

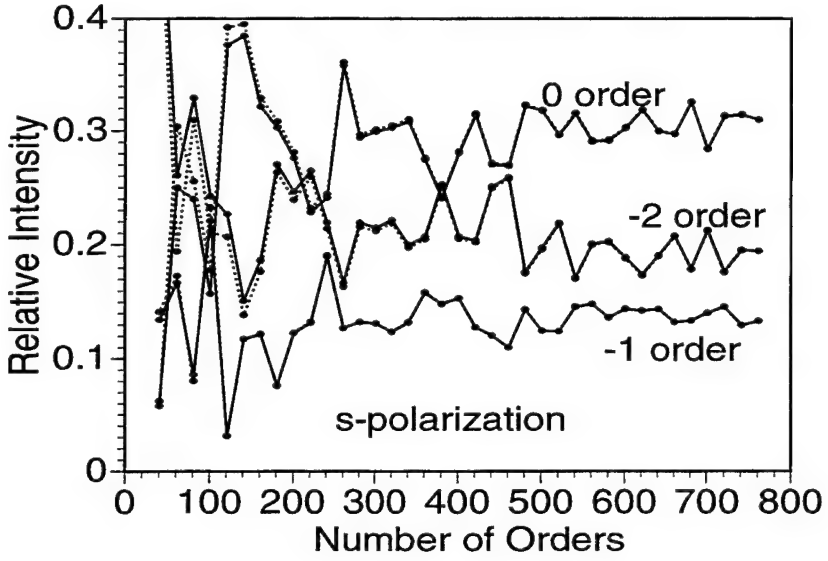


FIGURE 5. Relative TE-Polarized Diffraction Intensity of the Reflecting 0, −1, and −2 Orders Versus Number of Orders. This case is identical to Figure 4 except the incident beam is TE polarized.

For the deep grating considered in Figures 4 and 5, the convergence is much better if we change the permittivity from $\varepsilon_{sub}$ = (−48.91,4.2) to $\varepsilon_{sub}$ = (2.25,0) to represent a nonabsorbing dielectric. This grating is also discussed in References 1 and 2. For this case, Figures 6 and 7 show that the convergence is very good, in marked contrast to the metallic case. For this dielectric grating, Table 2 compares the results with those of References 1 and 2, and the agreement is excellent all around.

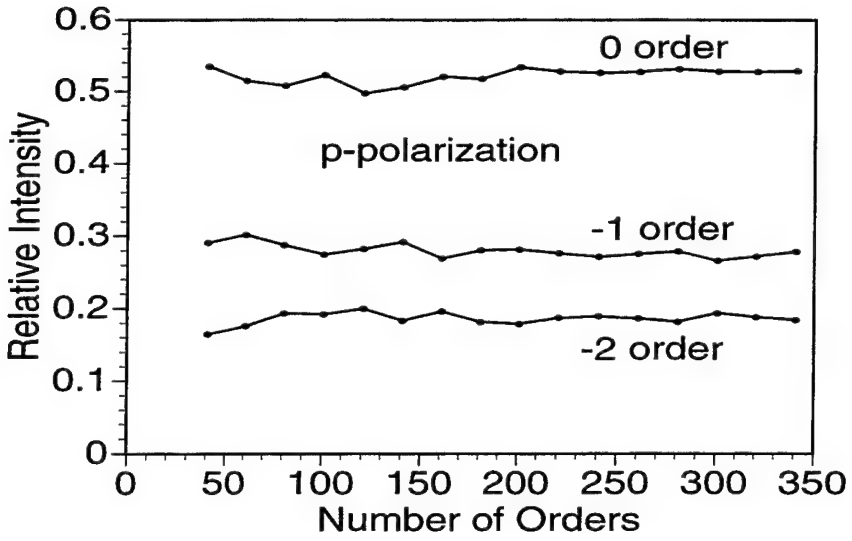


FIGURE 6. Relative TM-Polarized Diffraction Intensity for the Transmitting 0, −1, and −2 Orders Versus Number of Orders. The grating profile is sinusoidal and the material is a nonabsorbing dielectric with permittivity (2.25, 0). The grating height is $h = 17\lambda$, period $d = 1.7\lambda$, angle of incidence is 30 degrees, and the number of profile sublayers $n_z = 50$ This case is identical to Figure 4 except the substrate material is a dielectric, and the orders are transmitting.

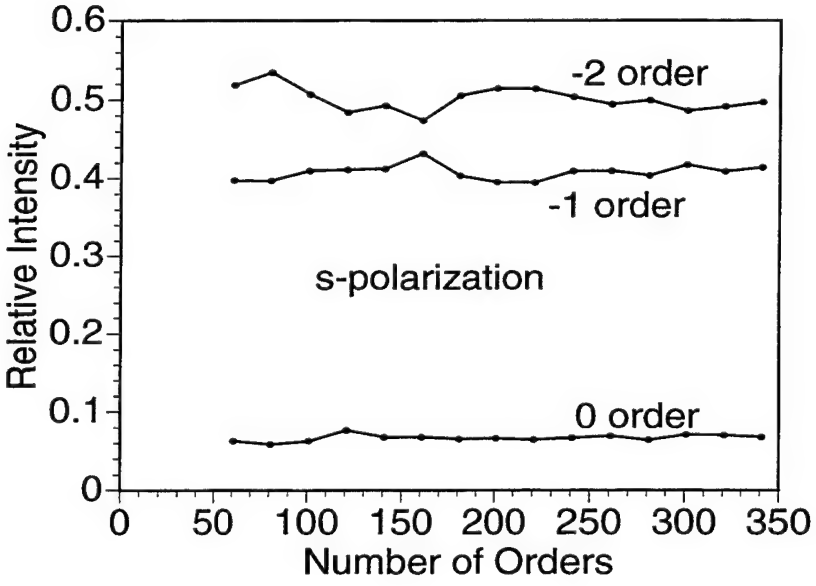


FIGURE 7. Relative TE-Polarized Diffraction Intensity for the Transmitting 0, −1, and −2 Orders Versus Number of Orders. This case is identical to Figure 6 except the incident beam is TE polarized.

TABLE 2. Transmission Diffraction Efficiencies Nonabsorbing Dielectric Sinusoidal Grating.

| | $h/d = 10$ | | |
|---|---|---|---|
| Order | 5 point *r*-space average | Our previous *k*-space | Li's |
| TE polarization | | | |
| -2 | 0.4940 | 0.4924 | 0.4974 |
| -1 | 0.4109 | 0.4113 | 0.4111 |
| 0 | 0.6846(-1) | 0.6982(-1) | 0.6750(-1) |
| TM polarization | | | |
| -2 | 0.1867 | 0.1905 | 0.1869 |
| -1 | 0.2744 | 0.2812 | 0.2757 |
| 0 | 0.5283 | 0.5185 | 0.5261 |

In conclusion, we described a real-space modal expansion **R**-matrix method, and we investigated the convergence versus number of diffracted orders. The method was still stable and works well for both TM and TE polarization with fast convergence for absorbing metal gratings with $h = 1.7\lambda$ ($h/d = 1$). For the same absorbing metallic grating 10 times deeper ($h = 17\lambda$), the method still stable for both TM and TE polarization, but the convergence appears to be quite slow with a damped oscillatory behavior. However, when the grating material is replaced by a dielectric, the convergence becomes quite rapid. We hope that future studies can identify the cause of slow convergence for the deep metallic grating.

## REFERENCES


1. J. M. Elson and P. Tran. "Dispersion and Diffraction in Photonic Media: A Different Modal Expansion for the **R**-Matrix Propagation Technique," *J. Opt. Soc. Am. A*, Vol. 12 (1995), pp. 1765-71.

2. L. Li. "Multilayer Modal Method for Diffraction Gratings of Arbitrary Profile, Depth, and Permittivity" *J. Opt. Soc. Am. A*, Vol. 10 (1993), pp. 2581-91.

3. J. Merle Elson and Phuc Tran. "Band Structure and Transmission of Photonic Media: A Real-Space Finite-Difference Calculation With the R-Matrix Propagator," in *Photonic Band Gap Materials*, ed. by Costas M. Soukoulis. Netherlands, Kluwer Academic Publishers, 1996. Pp. 341-54.

4. J. M. Elson and P. Tran. "A Coupled Mode Calculation With the R-Matrix Propagator for the Dispersion of Surface Waves on a Truncated Photonic Crystal," accepted *Phys. Rev. B*, (1996).

5. L. F. Desandre and J. M. Elson. "Extinction-Theorem Analysis of Siffraction Anomalies in Overcoated Gratings," *J. Opt. Soc. Am. A*, Vol. 8 (1990), pp. 763-777.

6. F. Montiel and M. Neviere. "Differential Theory of Gratings: Extension to Deep Gratings of Arbitrary Profile and Permittivity Through the **R**-matrix Propagation Algorithm," *J. Opt. Soc. Am. A*, Vol. 11 (1994), pp. 3241-50.

7. D. J. Zvijac and J. C. Light. "**R**-Matrix Theory for Collinear Chemical Reactions," *Chem. Phys.*, Vol. 12 (1976), pp. 237-51; J. C. Light and R. B. Walker. "An **R**-Matrix Approach to the Solution of Coupled Equations for Atom-Molecule Reactive Scattering," *J. Chem. Phys.*, Vol. 65 (1976), pp. 4272-82.

8. G. Tayeb. "Dispersion in Photonic Media and Diffraction From gratings: A Different Modal Expansion for the **R**-Matrix Propagation Technique: Comment," to be published in *J. Opt. Soc. Am. A* (MS # 5307).

## Appendix

In deriving Equation 1, finite-difference approximations of the $x$-derivatives were made. Consider the right-hand side of Equation 1a where the centered-derivative approximation

$$\frac{\partial}{\partial x}\left(\frac{1}{\varepsilon}\frac{\partial H_y}{\partial x}\right) \approx \frac{1}{(\Delta x)^2}\left\{\frac{H_y(x+\Delta x,z)-H_y(x,z)}{\varepsilon(x+\Delta x/2,z_c)}+\frac{H_y(x-\Delta x,z)-H_y(x,z)}{\varepsilon(x-\Delta x/2,z_c)}\right\} \quad \text{(A-1)}$$

has been used which is accurate to $O(\Delta x^2)$. This expression is obtained by writing the formulas

$$F(x+\Delta x/2) \approx F(x)+\frac{\Delta x}{2}F'(x)+\frac{1}{2}\left(\frac{\Delta x}{2}\right)^2 F''(x)+\frac{1}{6}\left(\frac{\Delta x}{2}\right)^3 F'''(x) \quad \text{(A-2)}$$

$$F(x-\Delta x/2) \approx F(x)-\frac{\Delta x}{2}F'(x)+\frac{1}{2}\left(\frac{\Delta x}{2}\right)^2 F''(x)-\frac{1}{6}\left(\frac{\Delta x}{2}\right)^3 F'''(x) \quad \text{(A-3)}$$

and solving for $F'(x)$ yields

$$F'(x) \approx \frac{F(x+\Delta x/2)-F(x-\Delta x/2)}{\Delta x}-\frac{F'''(x)}{3}\frac{1}{8}\Delta x^2 \quad . \quad \text{(A-4)}$$

This expression is clearly accurate to order $O(\Delta x^2)$. In Equation A-4 we may replace $\Delta x$ by $3\Delta x$ which yields

$$F'(x) \approx \frac{F(x+3\Delta x/2)-F(x-3\Delta x/2)}{3\Delta x}-\frac{F'''(x)}{3}\frac{9}{8}\Delta x^2 \quad . \quad \text{(A-5)}$$

We may now combine Equations A-4 and A-5 such that the $O(\Delta x^2)$ term vanishes and this yields an expression for $F'(x)$, which is accurate to order $O(\Delta x^4)$. This $O(\Delta x^4)$ formula may be applied twice to evaluate the left-hand side of Equation A-1. First we let

$F(x) \equiv H_y(x)$ and this yields an expression $F_1'(x) \approx \partial H_y / \partial x$. Applying the formula a second time with $F(x) \equiv (1/\varepsilon)F_1'(x)$ yields a fourth-order accurate finite-difference result $F_2'(x) = [(1/\varepsilon)F_1'(x)]' \approx (\partial / \partial x)[(1/\varepsilon)(\partial H_y / \partial x)]$ for the left-hand side of Equation A-1. An analogous procedure can be applied to the right-hand side of Equation 1c. We have used both the second and fourth order formulas in our numerical calculations. Unfortunately, however, no significant improvement in convergence was seen for the deep grating calculations considered here.

## INITIAL DISTRIBUTION

1 Commander in Chief, U. S. Pacific Fleet, Pearl Harbor (Code 325)
1 Commander, Third Fleet
1 Commander, Seventh Fleet
1 Naval War College, Newport
1 Headquarters, 497th IG/INT Falls Church (OUWG Chairman)
2 Defense Technical Information Center, Fort Belvoir
1 Center for Naval Analyses, Alexandria, VA (Technical Library)